$CaTMg_2$ and $CaTCd_2$ (T = Rh, Pd, Pt) with YPd_2Si-type Structure

Michael Johnscher[a], Marcel Kersting[a], Samir F. Matar[b], and Rainer Pöttgen[a]

[a] Institut für Anorganische und Analytische Chemie, Universität Münster, Corrensstrasse 30, 48149 Münster, Germany

[b] CNRS, Université de Bordeaux, ICMCB, 87 Avenue Dr. A. Schweitzer, F-33608 Pessac-Cedex, France

Reprint requests to R. Pöttgen. E-mail: pottgen@uni-muenster.de

Z. Naturforsch. **2013**, *68b*, 111 – 120 / DOI: 10.5560/ZNB.2013-2317
Received December 11, 2012

The intermetallic calcium compounds $CaTMg_2$ and $CaTCd_2$ (T = Rh, Pd, Pt) were obtained by high-frequency melting of the elements in sealed niobium ampoules or through reactions in muffle furnaces. The polycrystalline samples were characterized by powder X-ray diffraction. They crystallize with a site occupancy variant of YPd_2Si, a ternary ordered version of Fe_3C. The structures of $CaPdMg_2$ and $CaPdCd_2$ were refined from single-crystal diffractometer data: *Pnma*, $a = 792.2(2)$, $b = 803.4(2)$, $c = 572.0(1)$ pm, $wR2 = 0.0663$, 1621 F^2 values, 24 variables for $Ca_{0.94}PdMg_{2.06}$ and $a = 794.6(2)$, $b = 809.5(3)$, $c = 554.7(2)$ pm, $wR2 = 0.0301$, 819 F^2 values, 23 variables for $CaPdCd_2$. A small range of homogeneity was observed for $Ca_{1-x}PdMg_{2+x}$. The magnesium and cadmium atoms build up three-dimensional tetrahedral substructures (306 – 327 pm Mg–Mg and 307 – 317 pm Cd–Cd) that resemble hexagonal diamond, lonsdaleite. Together with the palladium atoms one obtains three-dimensional, covalently bonded $[PdMg_2]$ and $[PdCd_2]$ networks which leave cages for the calcium atoms. The latter are bonded to these networks *via* shorter Ca–Pd contacts (298 – 319 pm in $Ca_{0.94}PdMg_{2.06}$ and 295 – 312 pm in $CaPdCd_2$). The course of the interatomic distances is in line with calculated overlap populations. The $CaPdMg_2$, $SrPdMg_2$ and $CaRhIn_2$ structures are all derived from a $CaIn_2$-related subcell by an ordered filling of transition metal atoms into trigonal prisms. This leads to different herringbone patterns for the networks of puckered and elongated hexagons of magnesium and indium atoms.

Key words: Magnesium, Cadmium, Cementite Phases, Electronic Structure

Introduction

The structure of the S-phase precipitate $MgCuAl_2$ [1, 2] is the prototype for a series of aluminides, gallides, indides, and thallides ATX_2 where A can be a rare earth or alkaline earth element, and T is an electron-rich transition metal. The X atoms build up lonsdaleite-related networks, and the ATX_2 structures can formally be described as transition metal-filled versions of binary Zintl phases AX_2 ($CaIn_2$ type) [3]. Although the $MgCuAl_2$-type structure is typically formed for triels, recently also some magnesium and cadmium compounds, $RETMg_2$ and $RETCd_2$ have been reported [4 – 7]. This is an astonishing result, given that they contain rare networks of tetrahedraly coordinated magnesium and cadmium atoms.

Even more interesting is the result that $MgCuAl_2$-type compounds are formed with two different alkaline earth elements, as shown by the synthesis of $AETMg_2$ (AE = Ca, Sr; T = Pd, Ag, Pt, Au) and isotypic $SrTCd_2$ compounds [8]. To give an example, the magnesium atoms in $CaAuMg_2$ build up the orthorhombically distorted tetrahedral network, and the calcium atoms fill the typical cation position. Thus one observes clear segregation of magnesium and the heavier alkaline earth elements into different substructures without formation of a solid solution. This is similar to the situation in the calcium-rich compounds Ca_4AgMg and Ca_4AuMg [9].

The $MgCuAl_2$-type phases so far have been observed for valence electron concentrations in the range of 16 – 20 [10]; however, also size criteria play an important role. During our systematic phase analytical studies of the AE-T-Mg and AE-T-Cd systems with the heavier alkaline earth elements we obtained the new phases $CaTMg_2$ and $CaTCd_2$ (T = Rh, Pd, Pt). These calcium compounds crystallize with the closely related

YPd$_2$Si type [11], a ternary ordered version of the cementite structure, Fe$_3$C [12]. The synthesis, structure, and bonding peculiarities are reported herein.

Experimental

Synthesis

Starting materials for the syntheses of the CaTMg$_2$ and CaTCd$_2$ (T = Rh, Pd, Pt) samples were granules of distilled calcium (Johnson Matthey, > 99.5 %), palladium tear drops, rhodium and platinum sponge (Degussa-Hüls, > 99.9 % or Allgemeine Gold- und Silberscheideanstalt, Pforzheim, > 99.9 %), a magnesium rod (Johnson Matthey, Ø 16 mm, > 99.5 %; the surface of the rod was first cut on a turning lathe in order to remove surface impurities), and a cadmium rod (Johnson Matthey, > 99.9 %).

For the preparation of CaTMg$_2$ (T = Rh, Pd, Pt) pieces of calcium, the noble metal sponge or pieces and turnings of the magnesium rod were weighed in the ideal 1 : 1 : 2 atomic ratios and arc-welded [13] in small niobium tubes under an argon pressure of *ca.* 700 mbar. The argon was purified over titanium sponge (900 K), silica gel, and molecular sieves.

The niobium ampoules were sealed in a quartz tube for protection against oxidation and then annealed within 2 h to 1273 K in a muffle furnace. After keeping the temperature for 2 h it was lowered to 873 K within 5 h, kept at 873 K for another 30 h, followed by radiative heat loss. The samples were separated mechanically from the ampoules. No reactions with the ampoule material were evident. The polycrystalline samples are sensitive to moisture and were kept in Schlenk tubes.

The CaTCd$_2$ samples (T = Pd, Pt) were synthesized by a two-step procedure. First calcium, the noble metal and cadmium were weighed in 1 : 1 : 2.1 atomic ratios and arc-welded in small niobium tubes. The latter were placed in a water-cooled sample chamber of a high-frequency furnace (Hüttinger Elektronik, Freiburg, type TIG 1.5/300) [14] under flowing argon and annealed at 1300 K for about ten minutes, followed by cooling to 800 K within 30 min. Finally the samples were annealed for two hours at that tempera-

Compound	Structure type	a (pm)	b (pm)	c (pm)	V (nm^3)	Reference
Ca$_3$Pd	Fe$_3$C	769.9	993.7	669.1	0.5119	[44]
CaRhMg$_2$	YPd$_2$Si	787.0(1)	783.8(1)	571.0(1)	0.3522	this work
CaPdMg$_2$	YPd$_2$Si	792.2(2)	803.4(2)	572.0(1)	0.3641	this work
CaPtMg$_2$	YPd$_2$Si	788.5(2)	792.7(2)	566.5(1)	0.3541	this work
CaPdCd$_2$	YPd$_2$Si	794.6(2)	809.5(3)	554.7(2)	0.3568	this work
CaPtCd$_2$	YPd$_2$Si	796.6(3)	809.9(2)	552.6(2)	0.3565	this work

Table 1. Lattice parameters (Guinier powder data) of Ca$_3$Pd and compounds CaTMg$_2$ and CaTCd$_2$ (T = Rh, Pd, Pt). Standard deviations are given in parentheses.

Empirical formula	Ca$_{0.94(1)}$PdMg$_{2.06(1)}$	CaPdCd$_2$
Formula weight, g mol^{-1}	194.15	371.28
Unit cell dimension (Guinier powder data)		
a, pm	792.2(2)	794.6(2)
b, pm	803.4(2)	809.5(3)
c, pm	572.0(1)	554.7(2)
Cell volume V, nm^3	0.3641	0.3568
Calculated density, g cm^{-3}	3.54	6.91
Crystal size, μm^3	20 × 80 × 80	50 × 80 × 110
Transmission ratio (min / max)	0.349 / 0.799	0.332 / 0.580
Absorption coefficient, mm^{-1}	6.5	17.9
F(000), e	358	648
ω range; increment, deg	−60 – 190; 0.3	0 – 180; 1
Integration parameters A / B / EMS	6.7 / −6.2 / 0.012	11.6 / 1.7 / 0.011
θ range for data collection, deg	4 – 46	4 – 35
Range in hkl	±15, ±16, ±11	±12, ±12, ±8
Total no. of reflections	35970	5338
Independent reflections / R_{int}	1621 / 0.0581	819 / 0.0229
Reflections with $I > 2\sigma(I)$/R_σ	1191 / 0.0240	758 / 0.0131
Data / ref. parameters	1621 / 24	819 / 23
Goodness-of-fit on F^2	0.997	1.082
$R1$ / $wR2$ for $I > 2\sigma(I)$	0.0270 / 0.0653	0.0146 / 0.0295
$R1$ / $wR2$ for all data	0.0348 / 0.0663	0.0179 / 0.0301
Extinction coefficient	0.038(2)	0.0195(4)
Largest diff. peak / hole, e Å^{-3}	1.25 / −1.30	0.78 / −0.93

Table 2. Crystal data and structure refinement for Ca$_{0.94(1)}$PdMg$_{2.06(1)}$ and CaPdCd$_2$, space group $Pnma$, Z = 4.

ture, followed by quenching. The temperature was controlled through a Sensor Therm Methis MS09 pyrometer with an accuracy of ±30 K. These niobium ampoules were sealed in quartz tubes for protection against oxidation. Finally the ampoules were annealed in a muffle furnace at 823 K for one week. The CaTCd$_2$ samples are only weakly moisture sensitive

EDX data

Semiquantitative EDX analyses of the single crystals studied on the diffractometers were carried out in variable pressure mode with a Zeiss EVO® MA10 scanning electron microscope with wollastonite, palladium, magnesium oxide, and cadmium as standards. The experimentally observed average composition of 26 ± 1 at.-% Ca : 25 ± 1 at.-% Pd : 49 ± 1 at.-% Cd was close to the ideal one. For the magnesium-containing crystal both the refined (23.5 at.-% Ca : 25 at.-% Pd : 51.5 at.-% Mg) and the EDX analyses (21 ± 2 at.-% Ca : 22 ± 2 at.-% Pd : 57 ± 2 at.-% Mg) showed a slightly higher magnesium content, indicating a small range of homogeneity. The standard uncertainties account for the irregular shape of the crystal surfaces. No impurity elements were detected.

X-Ray diffraction

Basic characterization of the CaTMg$_2$ and CaTCd$_2$ (T = Rh, Pd, Pt) samples was carried out by powder X-ray diffraction using the Guinier technique: imaging plate detector, Fujifilm BAS-1800, Cu$K_{\alpha1}$ radiation, and α-quartz (a = 491.30, c = 540.46 pm) as an internal standard. The orthorhombic lattice parameters (Table 1) were deduced from least-squares refinements of the Guinier powder data. Correct indexing was ensured by comparison of the experimental patterns with calculated ones [15].

Crystal fragments of CaPdMg$_2$ and CaPdCd$_2$ were selected from the crushed samples annealed in the muffle furnaces. The crystals were first characterized on a Buerger camera (using white Mo radiation) to check their quality. Intensity data of a suitable CaPdCd$_2$ crystal were collected on a Stoe IPDS-II image plate system (graphite-monochromatized MoK_α radiation; λ = 71.073 pm) in oscillation mode. The CaPdMg$_2$ data set was measured on a Stoe Stadi Vari diffractometer equipped with a Mo micro focus source and a Pilatus detection system and scaled subsequently according to the Gaussian-shaped profile of the X-ray source. Numerical absorption corrections were applied to both data sets. Details about the data collections and the crystallographic parameters are summarized in Table 2.

Structure refinements

The diffractometer data sets of CaPdMg$_2$ and CaPdCd$_2$ showed primitive orthorhombic lattices, and the systematic extinctions were compatible with space group *Pnma*. The starting atomic parameters were deduced from Direct Methods with SHELXS-97 [16, 17], and the two structures were refined with anisotropic displacement parameters for all atoms with SHELXL-97 (full-matrix least-squares on F_o^2) [18, 19]. The refinements readily revealed isotypism with YPd$_2$Si [11], and in the following cycles the setting of the silicide was used. The occupancy parameters were refined in separate series of least-squares cycles for both data sets. The sites of CaPdCd$_2$ were fully occupied within two standard deviations, and the ideal composition was assumed again in the following cycles. The magnesium-based crystal showed too low scattering power for the 4c calcium site, indicating a small degree of mixed occupancy with magnesium. This mixed occupancy was refined as a least-squares variable in the following cycles, leading to the composition Ca$_{0.94(1)}$PdMg$_{2.06(1)}$ for the investigated crystal. The final difference Fourier syntheses revealed no residual peaks. The refined atomic positions, displacement parameters, and interatomic distances are given in Tables 3 – 5.

Table 3. Atomic coordinates and anisotropic displacement parameters (pm^2) for Ca$_{0.94(1)}$PdMg$_{2.06(1)}$ and CaPdCd$_2$. U_{eq} is defined as one third of the trace of the orthogonalized U_{ij} tensor. The parameters of idealized CaPdMg$_2$ obtained by geometry optimization are listed in italics.

Atom	Wyckoff site	x	y	z	U_{eq}
Ca$_{0.94(1)}$PdMg$_{2.06(1)}$					
Ca[a]	4c	0.03241(7) *0.033*	1/4	0.10005(10) *0.102*	221(2)
Pd	4c	0.37578(3) *0.377*	1/4	0.88544(4) *0.884*	215(1)
Mg	8d	0.16774(10) *0.169*	0.05683(9) *0.056*	0.60470(14) *0.604*	223(1)
CaPdCd$_2$					
Ca	4c	0.03320(8)	1/4	0.10208(10)	140(1)
Pd	4c	0.37781(3)	1/4	0.88151(4)	117(1)
Cd	8d	0.17207(2)	0.05570(2)	0.59466(3)	135(1)

[a] The calcium site shows mixed occupancy of 94(1) % Ca + 6(1) % Mg.

Table 4. Anisotropic displacement parameters (pm^2) for $Ca_{0.94(1)}PdMg_{2.06(1)}$ and $CaPdCd_2$.

Atom	U_{11}	U_{22}	U_{33}	U_{23}	U_{13}	U_{12}
$Ca_{0.94(1)}PdMg_{2.06(1)}$						
Ca[a]	208(2)	248(3)	207(3)	0	11(2)	0
Pd	200(1)	216(1)	229(1)	0	−10(1)	0
Mg	232(3)	200(3)	236(3)	−12(2)	−11(2)	−2(2)
$CaPdCd_2$						
Ca	125(2)	183(3)	112(2)	0	5(2)	0
Pd	116(1)	113(1)	121(1)	0	−6(1)	0
Cd	133(1)	116(1)	156(1)	−27(1)	−20(1)	2(1)

[a] The calcium site shows mixed occupancy of 94(1) % Ca + 6(1) % Mg.

Further details of the crystal structure investigation may be obtained from Fachinformationszentrum Karlsruhe, 76344 Eggenstein-Leopoldshafen, Germany (fax: +49-7247-808-666; E-mail: crysdata@fiz-karlsruhe.de, http://www.fiz-karlsruhe.de/request_for_deposited_data.html) on quoting the deposition number CSD-425508 ($Ca_{0.94}PdMg_{2.06}$) and CSD-425509 ($CaPdCd_2$).

Computational methods

Two computational methods within the DFT [20, 21] were used in a complementary manner. The Vienna *ab initio* simulation package (VASP) code [22, 23] allows geometry optimization and total energy calculations. For this we use the projector augmented wave (PAW) method [23, 24], built within the generalized gradient approximation (GGA) scheme following Perdew, Burke and Ernzerhof (PBE) [25]. Also preliminary calculations with local density approximation LDA [26] led to an underestimated volume *versus* the experiment. The conjugate-gradient algorithm [27] is used in this computational scheme to relax the atoms. The tetrahedron method with Blöchl corrections [24] as well as a Methfessel-Paxton [28] scheme were applied for both geometry relaxation and total energy calculations. Brillouin zone (BZ) integrals were approximated using the special k-point sampling. The optimization of the structural parameters was performed until the forces on the atoms were less than 0.02 eV Å^{-1} and all stress components less than 0.003 eV Å^{-3}. The calculations are converged at an energy cut-off of 400 eV for the plane-wave basis set with respect to the k-point integration with a starting mesh of $4 \times 4 \times 4$ up to $8 \times 8 \times 8$ for best convergence and relaxation to zero strains. The calculations are scalar-relativistic and assume spin-degenerate total spins.

Then all-electron calculations with the GGA were carried out for a full description of the electronic structure and the properties of chemical bonding, using the full potential scalar-relativistic augmented spherical wave (ASW) method [29, 30]. In the minimal ASW basis set, we chose the outermost shells to represent the valence states, and the matrix elements were constructed using partial waves up to $l_{max} + 1 = 3$ for Pd and $l_{max} + 1 = 2$ for Ca and Mg. Self-consistency was achieved when charge transfers and energy changes between two successive cycles were below 10^{-8} and 10^{-6} eV, respectively. BZ integrations were performed using the linear tetrahedron method within the irreducible wedge. Besides the site projected density of states, we have discussed qualitatively the pair interactions based on the overlap population analysis with the crystal orbital overlap population (COOP) [31]. In the plots, positive, negative, and zero COOP indicate bonding, anti-bonding, and non-bonding interactions, respectively.

Table 5. Interatomic distances (pm) in the structures of $Ca_{0.94}PdMg_{2.06}$ and $CaPdCd_2$. All distances of the first coordination spheres are listed. Standard deviations are all smaller or equal than 0.2 pm.

$Ca_{0.94}PdMg_{2.06}$				$CaPdCd_2$			
Ca[a]:	1	Pd	298.4	Ca:	1	Pd	295.3
	1	Pd	304.2		1	Pd	299.9
	1	Pd	319.4		1	Pd	311.9
	2	Mg	338.3		2	Cd	334.0
	2	Mg	340.4		2	Cd	340.7
	2	Mg	342.3		2	Cd	340.8
	2	Mg	344.8		2	Cd	340.8
	2	Mg	348.2		2	Cd	345.0
Pd:	2	Mg	277.6	Pd:	2	Cd	277.1
	2	Mg	278.6		2	Cd	277.1
	2	Mg	278.7		2	Cd	282.1
	1	Ca	298.4		1	Ca	295.3
	1	Ca	304.2		1	Ca	299.9
	1	Ca	319.4		1	Ca	311.9
Mg:	1	Pd	277.6	Cd:	1	Pd	277.1
	1	Pd	278.6		1	Pd	277.1
	1	Pd	278.7		1	Pd	282.1
	1	Mg	305.5		1	Cd	306.5
	1	Mg	310.4		1	Cd	314.6
	2	Mg	327.3		2	Cd	316.9
	1	Ca	338.3		1	Ca	334.0
	1	Ca	340.4		1	Ca	340.7
	1	Ca	342.3		1	Ca	340.8
	1	Ca	344.8		1	Ca	340.8
	1	Ca	348.2		1	Ca	345.0

[a] The calcium site shows mixed occupancy of 94(1) % Ca + 6(1) % Mg.

Discussion

Crystal chemistry

The new calcium compounds Ca*T*Mg$_2$ and Ca*T*Cd$_2$ (*T* = Rh, Pd, Pt) crystallize with the orthorhombic YPd$_2$Si-type structure (space group *Pnma*) [11], a ternary ordered variant of the well known cementite type, Fe$_3$C [12]. So far, the YPd$_2$Si type has been observed for *RE*Pd$_2$Si and *RE*Pt$_2$Si silicides [11, 32 – 34], *RE*Pd$_2$Ge germanides [35 – 39], UAu$_2$Al [40], CePd$_2$Ga [41], YPd$_2$Ga [42], and the phosphide MgNi$_2$P [43]. In these intermetallics, the small silicon, germanium, aluminum, gallium, or phosphorus atoms fill trigonal-prismatic sites. The inverse ordering pattern is realized in the magnesium and cadmium compounds reported herein. The transition metal atoms fill trigonal-prismatic sites formed by the magnesium, respectively cadmium atoms. As an example for the new ternary phases we discuss the CaPdMg$_2$ structure.

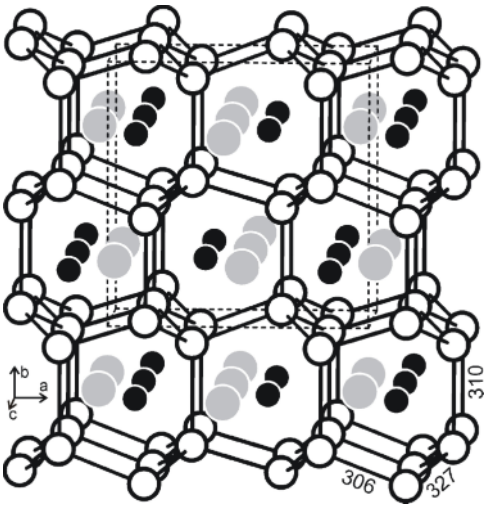

Fig. 1. View of the CaPdMg$_2$ structure approximately along the crystallographic *c* axis. Calcium, palladium and magnesium atoms are drawn as medium grey, black filled and open circles, respectively. The three-dimensional lonsdaleite-related magnesium network is emphasized. Relevant Mg–Mg distances are indicated.

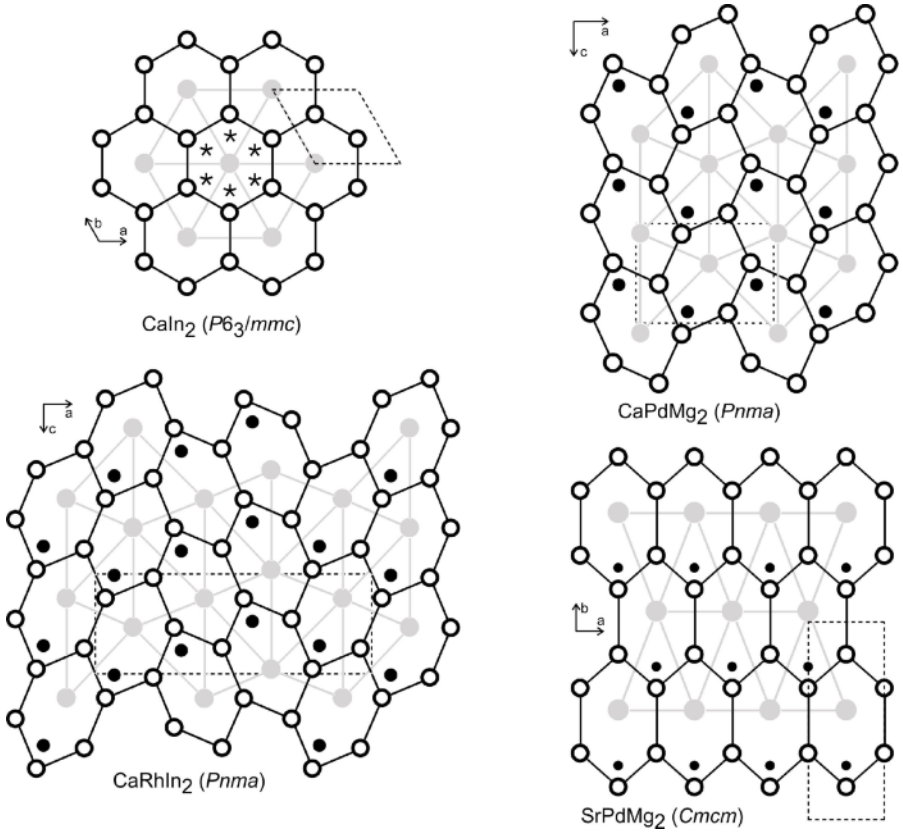

Fig. 2. View upon one puckered indium or magnesium layer and its adjacent calcium (strontium) layer in the structures of CaIn$_2$, CaRhIn$_2$, CaPdMg$_2$, and SrPdMg$_2$. Calcium (strontium), rhodium (palladium) and indium (magnesium) atoms are drawn as medium grey, black filled and open circles, respectively. The three ternary structures arise from different insertion of the transition metal atoms into distorted CaIn$_2$-type subcells as emphasized by grey lines (the ideal interstitial sites in CaIn$_2$ are marked with asterisks; within one hexagon of the ternaries only one position is filled).

The single-crystal X-ray diffraction data for CaPdMg$_2$ revealed a small homogeneity range Ca$_{1-x}$PdMg$_{2+x}$. In this context it is interesting to note that binary Ca$_3$Pd [44] with cementite structure is known, while related binaries are not known for the corresponding Ca-Rh and Ca-Pt systems. The refined composition of the single crystal was Ca$_{0.94}$PdMg$_{2.06}$. One can thus assume an extension towards higher and lower calcium contents as well. Detailed preparative work on these solid solutions is in progress. From Table 1 it becomes clear that substitution of calcium by the smaller magnesium atoms leads to anisotropic changes of the lattice parameters, *i. e.* the *a* parameter is increasing, while *b* and *c* are decreasing. Towards the magnesium-rich side one can expect a change in structure type since binary Mg$_3$Pd [45] crystallizes with the hexagonal Cu$_3$P type.

A view of the CaPdMg$_2$ structure approximately along the *c* axis is presented in Fig. 1. Similar to the MgCuAl$_2$-type phases [8, 10], for CaPdMg$_2$ we also observe formation of a pronounced lonsdaleite-related (hexagonal diamond) magnesium substructure. The Mg–Mg distances range from 306 to 327 pm, in close agreement with the average Mg–Mg distance of 320 pm in *hcp* magnesium [46]. We can thus expect substantial Mg–Mg bonding. In the magnesium substructures of the MgCuAl$_2$-type phases one observes much longer Mg–Mg distances and larger anisotropy in Mg–Mg bonding [8].

The shortest distances within the CaPdMg$_2$ structure occur between the palladium and magnesium atoms. Within the distorted trigonal PdMg$_6$ prisms the Pd–Mg distances range from 278 to 279 pm, slightly longer than the sum of the covalent radii of 264 pm [47]. Together the palladium and magnesium atoms build up a complex three-dimensional [PdMg$_2$] network which leaves cavities for the calcium atoms. The latter have coordination number 13 with three palladium and ten magnesium atoms in their coordination shell. The calcium atoms are bonded to the [PdMg$_2$] network through short Ca–Pd bonds (298 – 319 pm), close in length to the sum of the covalent radii of 302 pm. A similar bonding situation occurs also in CaPdIn$_2$ (294 – 316 pm Ca–Pd) [48] and CaPdSn$_2$ (305 pm) [49].

At large, one observes similar structural features for the MgCuAl$_2$- and YPd$_2$Si-type *AET*Mg$_2$ compounds. But what is the difference between the two types? The *CaMg*$_2$ substructures of both families resemble the hexagonal Zintl phase CaIn$_2$. This relationship was first reported for the indides Sr*T*In$_2$ (*T* = Rh, Pd, Ir, Pt) [3]. In Fig. 2 we present cut-outs of the CaIn$_2$ [50], CaPdMg$_2$, CaRhIn$_2$ [51], and SrPdMg$_2$ structures [8]. For each compound one layer of puckered hexagons and one *Ca*, *CaPd*, *CaRh*, and *SrPd* layer are shown. We start the structural comparison with the *unfilled* hexagonal CaIn$_2$ type. This structure leaves six possible sites (marked by asterisks) for the incorporation of the transition metal atom. For geometric reasons, only one of these sites is filled per hexagon, and adjacent sites between two hexagons cannot be occupied simultaneously. With the three structures presented in Fig. 2 one knows three different coloring variants. In all of these compounds the puckered hexagons are elongated as a consequence of the Pd–Mg and Rh–In bonding. The elongated hexagons all point to one direction in SrPdMg$_2$, while CaPdMg$_2$ and CaRhIn$_2$ show simple and double herringbone patterns. The different coloring variants allow for the formation of 1-1-2 compounds for diverse element combinations and valence electron concentrations (VEC). The YPd$_2$Si-type Ca*T*Mg$_2$ compounds reported herein have low VEC of 15 and 16, while the MgCuAl$_2$-type compounds show a range from 16 to 20. Further phase analytical work on the Ba-*T*-Mg and Ba-*T*-Cd systems is under way in order to elucidate potential 1-1-2 compounds with much larger cations.

Geometry optimization results and discussions

In Table 3 the calculated positional parameters for CaPdMg$_2$ show good agreement with the experimental data but tend to provide a slightly lower volume. We further derive the equilibrium zero pressure parameters from the energy-volume, $E(V)$, equation of state (EOS) with calculations around minima found from geometry optimization. The resulting values are plotted in Fig. 3 using a 3rd order Birch EOS [52] providing E_0, V_0, B_0 and B', respectively, as the equilibrium energy, the volume, the bulk modulus and its pressure derivative given in the insert. The fit curves produce a slightly larger volume *versus* experiment and hence correct the calculated value from geometry optimization because GGA tends to provide larger volumes and a certain underbinding, contrary to the LDA. The bulk modulus which translates the resistance of the compound to isotropic compression has a very low value of $B_0 = 48$ GPa. Compared with the constituent ele-

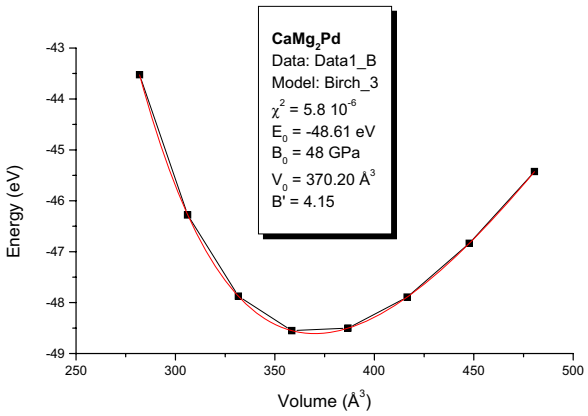

Fig. 3 (color online). CaPdMg$_2$: Energy-volume curve and fit values from Birch EOS. χ^2: goodness of fit.

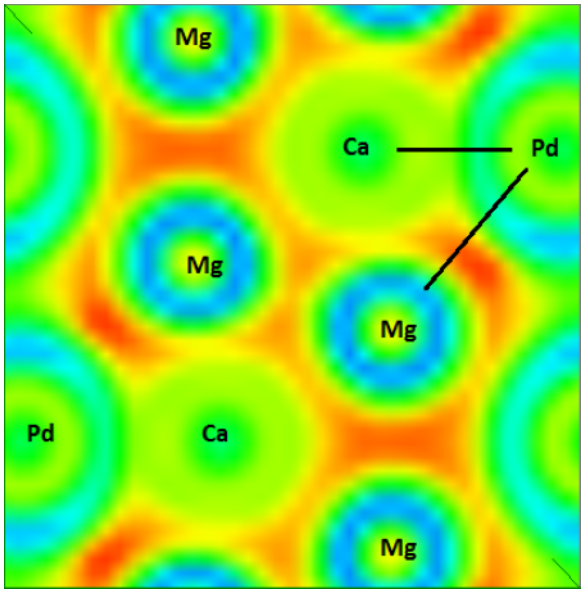

Fig. 4 (color online). CaPdMg$_2$: Electron localization function ELF projection onto the *ab* plane highlighting the Ca–Pd and Mg–Pd bonds and the localization (red spots) along Mg–Mg. Also notice the dominant green ELF indicating free electron-like behavior (see text for color definitions).

ments in GPa units, B_0(Pd) = 180, B_0(Mg) = 45 GPa and B_0(Ca) = 17, it cannot be the consequence of their averaging (96 GPa) but should rather arise from the nature of its electronic structure.

A first impression is given by the mapping of the electron localization function (ELF) [53]. ELF is a normalized (unit-less) function: $0 < \mathrm{ELF} < 1$, with ELF = 0 indicating zero localization (blue contours), ELF = 1 for strong localization (red contours) and ELF = 1/2 value for free electron gas behavior (green contours). The plot shown in Fig. 4 is for a plane cross-

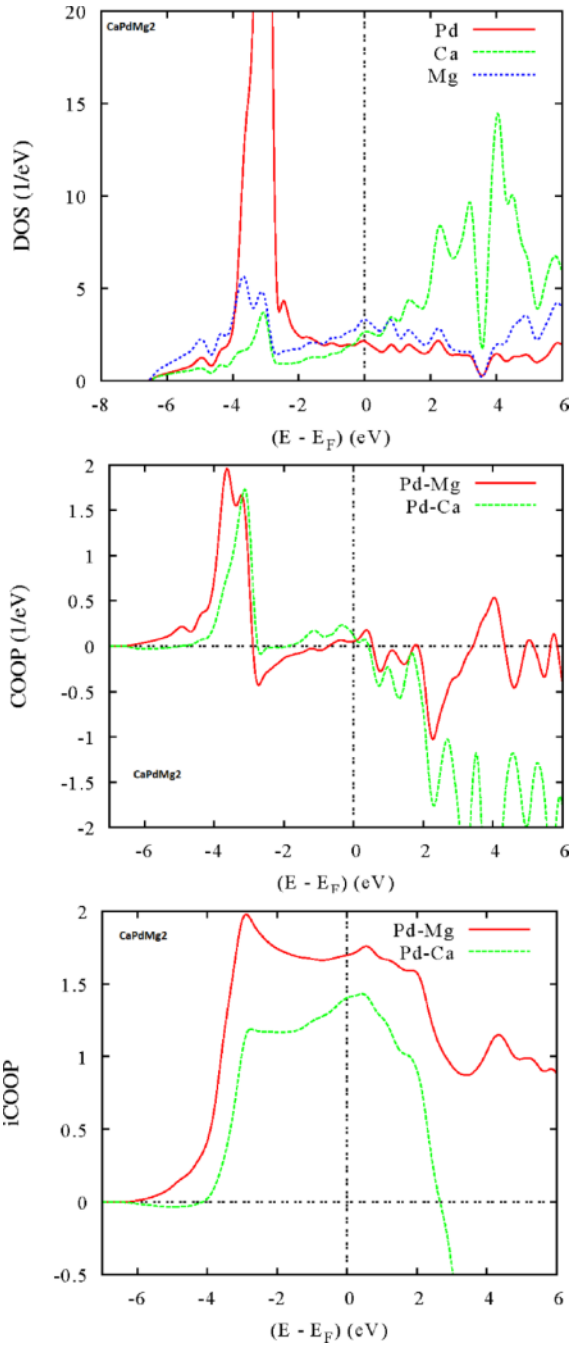

Fig. 5 (color online). Electronic structure and chemical bonding in CaPdMg$_2$.

ing the Mg atoms. The departure of electrons from electropositive Ca and Mg is shown by blue areas (zero localization spots), not seen for Ca because, the atoms are not in the same plane. Nevertheless the dominating green color indicates a free electron itinerant (s, p) behavior, despite the presence of low-energy lying Pd d states in the valence band. The highlighted Mg–Pd and Ca–Pd bonds show rather different features with localized ELF (red-like spots) between Mg and Pd and only green contours between Ca and Pd. The red spots in between Mg and neighboring Pd atoms are a relevant feature and indicate bonding properties discussed in the next section.

We further analyze the charge density issued from the self consistent calculations using the AIM (atoms in molecules theory) approach [54] developed by Bader who devised an intuitive way of splitting molecules into atoms as based purely on the electronic charge density. Typically in chemical systems, the charge density reaches a minimum between atoms and this is a natural region to separate them from each other. Such an analysis does not constitute a tool for evaluating absolute ionizations. Bader's analysis is done using a fast algorithm operating on a charge density grid. The program [55] reads in charge densities obtained from high precision VASP calculations and outputs the total charge associated with each atom. Further, in order to include core electrons within the PAW method in VASP, use is made of the LAECHG = .TRUE. parameter in the 'INCAR' control file followed by operating a summation of core and valence charge densities using a simple *perl* program [55]. The results of computed charge changes (ΔQ) are such that they lead to neutrality when the respective multiplicities are accounted for; the obtained values are:

$$\Delta Q(\mathrm{Mg}) = +0.236;\ \Delta Q(\mathrm{Ca}) = +0.919 \text{ and}$$
$$\Delta Q(\mathrm{Pd}) = -1.391\,.$$

Due to the large electronegativity difference between Pd ($\chi = 2.2$) on one hand and Mg ($\chi = 1.3$) and Ca ($\chi = 1.0$) on the other, charge transfer is observed from Ca and Mg (positive charge) towards Pd (negative charge). However, the more pronounced electropositive character of calcium leads to a more extensive ionization (close to 1) while Mg is much less ionized. This corroborates the ELF plots described above and indicates a rather iono-covalent Mg–Pd compared to a more ionic Ca–Pd bond. The charge distribution and the course of the bond strengths resemble those in CaAuIn$_2$ [48].

Electronic structure and chemical bonding

The electronic density of states and the chemical bonding are analyzed based on experimental data and assuming a spin-degenerate total spin (NSP) configuration. At self consistent convergence the charge transfer follows the trends observed above.

Figure 5 shows the site projected density of states (PDOS) for CaPdMg$_2$ accounting for site multiplicities and the total number of FU per cell. Along the x axis the energy is with respect to the Fermi level E_F. The valence band is dominated by low energy filled Pd-d states with contributions from Mg and Ca PDOS underneath, pointing to quantum mixing between them. The twice larger number of Mg *vs*. Ca leads to higher PDOS, but most of the Ca PDOS are empty and found above E_F in the conduction band. This is in agreement with the larger ionization of Ca as detailed above. The crossing of E_F by low intensity itinerant broad PDOS from all components signals a metal with mainly s character orbitals.

The quantum mixing between Pd and Ca/Mg can be further assessed using the COOP criterion of chemical bonding. The relative strengths of chemical bonding can be discussed within the valence band below E_F with one atom of each kind for the sake of comparing magnitudes. The Mg–Pd bond is found with larger intensity than the Ca–Pd bond with main contributions below the Pd-d PDOS. This follows from the larger Ca–Pd *vs*. Mg–Pd distances (298 *vs*. 278 pm). Low magnitude antibonding COOP (<0) are observed around −2 eV, but they do not change the trend of stronger Mg–Pd bonding. This is shown with the integrated *i*COOP criterion in 3$^{\mathrm{rd}}$ panel to be interpreted by the principle: the larger the area below the curve, the stronger the bonding.

Acknowledgement

We thank Dipl.-Ing. U. Ch. Rodewald for the intensity data collections. This work was supported by the Deutsche Forschungsgemeinschaft.

[1] H. Perlitz, A. Westgren, *Ark. Kemi, Mineral. Geol. B* **1943**, *16*, 1.
[2] B. Heying, R.-D. Hoffmann, R. Pöttgen, *Z. Naturforsch.* **2005**, *60b*, 491.
[3] R.-D. Hoffmann, U.Ch. Rodewald, R. Pöttgen, *Z. Naturforsch.* **1999**, *54b*, 38.
[4] M. E. Kost, A. L. Shilov, N. T. Kusnetsov, *Russ. J. Inorg. Chem.* **1988**, *33*, 467.
[5] G. Renaudin, L. Guénée. K. Yvon, *J. Alloys Compd.* **2003**, *350*, 145.
[6] A. Doğan, D. Johrendt, R. Pöttgen, *Z. Anorg. Allg. Chem.* **2005**, *631*, 451.
[7] M. Kersting, R. Pöttgen, *Z. Naturforsch.* **2011**, *66b*, 651.
[8] M. Kersting, M. Johnscher, S. F. Matar, R. Pöttgen, *Z. Anorg. Allg. Chem.* **2013**, *639*, submitted for publication.
[9] M. Kersting, S. F. Matar, C. Schwickert, R. Pöttgen, *Z. Naturforsch.* **2012**, *67b*, 61.
[10] R. Pöttgen, M. Lukachuk, R.-D. Hoffmann, *Z. Kristallogr.* **2006**, *221*, 435.
[11] J. M. Moreau, J. Le Roy, D. Paccard, *Acta Crystallogr. B* **1982**, *38*, 2446.
[12] F. H. Herbstein, J. Smuts, *Acta Crystallogr.* **1964**, *17*, 1331.
[13] R. Pöttgen, Th. Gulden, A. Simon, *GIT Labor-Fachzeitschrift* **1999**, *43*, 133.
[14] R. Pöttgen, A. Lang, R.-D. Hoffmann, B. Künnen, G. Kotzyba, R. Müllmann, B. D. Mosel, C. Rosenhahn, *Z. Kristallogr.* **1999**, *214*, 143.
[15] K. Yvon, W. Jeitschko, E. Parthé, *J. Appl. Crystallogr.* **1977**, *10*, 73.
[16] G. M. Sheldrick, SHELXS-97, Program for the Solution of Crystal Structures, University of Göttingen, Göttingen (Germany) **1997**.
[17] G. M. Sheldrick, *Acta Crystallogr.* **1990**, *A46*, 467.
[18] G. M. Sheldrick, SHELXL-97, Program for the Refinement of Crystal Structures, University of Göttingen, Göttingen (Germany) **1997**.
[19] G. M. Sheldrick, *Acta Crystallogr.* **2008**, *A64*, 112.
[20] P. Hohenberg, W. Kohn, *Phys. Rev.* **1964**, *136*, B864.
[21] W. Kohn, L. J. Sham, *Phys. Rev.* **1965**, *140*, A1133.
[22] G. Kresse, J. Furthmüller, *Phys. Rev. B* **1996**, *54*, 11169.
[23] G. Kresse, J. Joubert, *Phys. Rev. B* **1999**, *59*, 1758; http://cms.mpi.univie.ac.at/vasp/vasp/IBRION_5_IBRION_6.html .
[24] P. E. Blöchl, *Phys. Rev. B* **1994**, *50*, 17953.
[25] J. P. Perdew, K. Burke, M. Ernzerhof, *Phys. Rev. Lett.* **1996**, *77*, 3865.
[26] D. M. Ceperley, B. J. Alder, *Phys. Rev. Lett.* **1980**, *45*, 566.
[27] W. H. Press, B. P. Flannery, S. A. Teukolsky, W. T. Vetterling, *Numerical Recipes*, Cambridge University Press, New York, **1986**.
[28] M. Methfessel, A. T. Paxton, *Phys. Rev. B* **1989**, *40*, 3616.
[29] A. R. Williams, J. Kübler, C. D. Gelatt, Jr., *Phys. Rev. B* **1979**, *19*, 6094.
[30] V. Eyert, *The Augmented Spherical Wave Method – A Comprehensive Treatment*, Lecture Notes in Physics, Springer, Heidelberg, **2007**.
[31] R. Hoffmann, *Angew. Chem., Int. Ed. Engl.* **1987**, *26*, 846.
[32] J. M. Kurenbaeva, Yu. D. Seropegin, O. I. Bodak, V. N. Nikiforov, *J. Alloys Compd.* **2000**, *299*, 235.
[33] M. Kolenda, M. Hofmann, B. Penc, A. Szytula, *Physica B* **2004**, *350*, e191.
[34] R. Rawat, I. Das, *J. Phys.: Condens. Matter* **2006**, *18*, 1051.
[35] J. L. Jorda, M. Ishikawa, E. Hovestreydt, *J. Less-Common Met.* **1983**, *92*, 155.
[36] Z. M. Barakatova, Y. D. Seropegin, O. I. Bodak, B. D. Belan, *Russ. Metall.* **1995**, *1*, 150.
[37] O. I. Bodak, O. L. Sologub, *Inorg. Mater.* **1992**, *27*, 2195.
[38] O. L. Sologub, P. S. Salamakha, *J. Alloys Compd.* **1999**, *291*, 181.
[39] Yu. D. Seropegin, A. V. Gribanov, O. I. Bodak, *J. Alloys Compd.* **1998**, *269*, 157.
[40] T. Takabatake, H. Iwasaki, H. Fujii, S.-I. Ikeda, S. Nishigori, Y. Aoki, T. Suzuki, T. Fujita, *J. Phys. Soc. Jpn.* **1992**, *61*, 778.
[41] B. Xue, H. Schwer, F. Hulliger, *Z. Kristallogr.* **1994**, *209*, 707.
[42] O. R. Myakush, A. O. Fedorchuk, *Visn. Lviv Derzh. Univ. (Ser. Khim.)* **2000**, *39*, 21.
[43] V. Keimes, A. Mewis, *Z. Naturforsch.* **1994**, *49b*, 1071.
[44] A. Palenzona, P. Manfrinetti, *J. Less-Common Met.* **1982**, *85*, 307.
[45] J. P. A. Makongo, C. Kudla, Yu. Prots, R. Niewa, U. Burkhardt, G, Kreiner, *Z. Kristallogr. NCS* **2005**, *220*, 289.
[46] J. Donohue, *The Structures of the Elements*, Wiley, New York **1974**.
[47] J. Emsley, *The Elements*, Oxford University Press, Oxford **1999**.
[48] R.-D. Hoffmann, R. Pöttgen, G. A. Landrum, R. Dronskowski, B. Künnen, G. Kotzyba, *Z. Anorg. Allg. Chem.* **1999**, *625*, 789.
[49] R.-D. Hoffmann, D. Kußmann, U.Ch. Rodewald, R. Pöttgen, C. Rosenhahn, B. D. Mosel, *Z. Naturforsch.* **1999**, *54b*, 709.
[50] A. Iandelli, *Z. Anorg. Allg. Chem.* **1964**, *330*, 221.

[51] R.-D. Hoffmann, R. Pöttgen, *Z. Anorg. Allg. Chem.* **2000**, *626*, 28.
[52] F. Birch, *J. Geophys. Res.* **1978**, *83*, 1257.
[53] A. D. Becke, K. E. Edgecombe, *J. Chem. Phys.* **1990**, *92*, 5397.
[54] R. Bader, *Chem. Rev.* **1991**, *91*, 893, and http://theory.cm.utexas.edu/bader/.
[55] Web references for VASP and Bader charge analysis: http://cms.mpi.univie.ac.at/vasp/vasp/Contents.html; http://theory.cm.utexas.edu/vtsttools/bader/vasp.php.